Title
Complex Evolution of Built-in Potential in Compositionally-Graded PbZr1–x Ti x O3 Thin Films

Journal
ACS Nano, 9(7)

ISSN
1936-0851

Authors
Agar, Joshua C
Damodaran, Anoop R
Velarde, Gabriel A
et al.

Publication Date
2015-07-28

DOI
10.1021/acsnano.5b02289

Peer reviewed

Complex Evolution of Built-in Potential in Compositionally-Graded $PbZr_{1-x}Ti_xO_3$ Thin Films

Joshua C. Agar,[†,‡] Anoop R. Damodaran,[†] Gabriel A. Velarde,[‡] Shishir Pandya,[†] R. V. K. Mangalam,[†] and Lane W. Martin*[,†,‡,§]

[†]Department of Materials Science and Engineering, University of California, Berkeley, Berkeley, California 94720, United States, [‡]Department of Materials Science and Engineering, University of Illinois, Urbana—Champaign, Urbana, Illinois 61801, United States, and [§]Materials Science Division, Lawrence Berkeley National Laboratory, Berkeley, California 94720, United States

ABSTRACT Epitaxial strain has been widely used to tune crystal and domain structures in ferroelectric thin films. New avenues of strain engineering based on varying the composition at the nanometer scale have been shown to generate symmetry breaking and large strain gradients culminating in large built-in potentials. In this work, we develop routes to deterministically control these built-in potentials by exploiting the interplay between strain gradients, strain accommodation, and domain formation in compositionally graded $PbZr_{1-x}Ti_xO_3$ heterostructures. We demonstrate that variations in the nature of the compositional gradient and heterostructure thickness can be used to control both the crystal and domain structures and give rise to nonintuitive evolution of the built-in potential, which does not scale directly with the magnitude of the strain gradient as would be expected. Instead, large built-in potentials are observed in compositionally-graded heterostructures that contain (1) compositional gradients that traverse chemistries associated with structural phase boundaries (such as the morphotropic phase boundary) and (2) ferroelastic domain structures. In turn, the built-in potential is observed to be dependent on a combination of flexoelectric effects (*i.e.*, polarization—strain gradient coupling), chemical-gradient effects (*i.e.*, polarization—chemical potential gradient coupling), and local inhomogeneities (in structure or chemistry) that enhance strain (and/or chemical potential) gradients such as areas with nonlinear lattice parameter variation with chemistry or near ferroelastic domain boundaries. Regardless of origin, large built-in potentials act to suppress the dielectric permittivity, while having minimal impact on the magnitude of the polarization, which is important for the optimization of these materials for a range of nanoapplications from vibrational energy harvesting to thermal energy conversion and beyond.

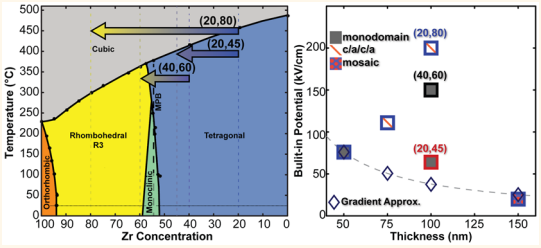

KEYWORDS: ferroelectrics · $PbZr_{1-x}Ti_xO_3$ · thin films · compositionally-graded heterostructures · permittivity

Susceptibility to electric field, stress, and temperature make ferroelectrics ideal candidates for a wide variety of nanoscale applications ranging from memories,[1] to actuators, to infrared sensors, to pyroelectric electron emitters.[2−4] The response of a ferroelectric is strongly coupled to both its atomic-scale crystal and nanoscale domain structures wherein small perturbations to either can dramatically influence the properties. The implementation of modern thin-film deposition techniques and increased availability of lattice-matched substrates has enabled the use of epitaxial strain to manipulate the crystal and domain structure of these materials and provides a means to tune susceptibilities.[5] In recent years, there has been recognition that epitaxial strain need not be homogeneous in nature, and researchers have looked to leverage the ability to deterministically create inhomogeneous strains to further control materials.[6−11] The presence of strain gradients are particularly interesting in ferroelectrics because of the potential for strong so-called flexoelectric effects. Flexoelectricity refers to the linear coupling of a strain gradient ($\partial\varepsilon_{ij}/\partial_{xk}$) and the polarization ($P_i$) of a material, mediated by the fourth-rank flexoelectric tensor (μ_{ijkl}). Bolstered by the ability to produce large strain gradients, on the order of 10^5 m^{-1}, in thin films through the use of mechanical stress,[12−14] defect and domain engineering,[8,9,15,16] and compositional gradients,[6,7] there has been a reemergence of interest in flexoelectricity. Such large strain gradients produce large

* Address correspondence to lwmartin@berkeley.edu.

Received for review April 16, 2015 and accepted June 30, 2015.

Published online June 30, 2015
10.1021/acsnano.5b02289

flexoelectric effects (or effects that mimic those arising from flexoelectricity) that can alter the ferroic response of materials,[17,18] allow for mechanically induced ferroelectric switching,[12−14] drive horizontal shifts of ferroelectric hysteresis loops,[7,19−21] and allow for independent tuning of typically coupled ferroelectric susceptibilities.[6,7,10]

Despite this renewed interest, there is widespread dissensus regarding how to define, quantify, measure, and/or decouple flexoelectric effects from other coupled electromechanical responses. In this context, there are discrepancies as to the magnitude and even the sign of flexoelectric coefficients in materials,[18] wherein experimentally measured values[22−25] are typically orders of magnitude larger than those predicted from first principles.[26−28] There is growing concern that additional contributions that can mimic flexoelectric response (which are unable to be decoupled in macroscale measurement, but are excluded from first-principles calculations) could possibly account for these discrepancies. These ancillary contributions include: strain-gradient-driven inhomogeneous segregation of space charges,[15,29] chemical gradients,[20,21,30] localized potential gradients at nanodomain boundaries,[31,32] polarization gradients (in the presence of screening charges which minimize depolarization),[33] surface piezoelectricity,[17,34,35] *etc*. Only recently has there been a concerted effort to understand the relative importance of the intrinsic flexoelectric and such ancillary contributions to the macroscopic response of materials. While the relative importance of these contributions is scientifically significant, what is most important from an engineering perspective is to understand how to maximize the collective influence of all these effects on the property of interest, in this case the built-in potential.

Here, we explore deterministic routes to control the macroscale built-in potential (*i.e.*, the horizontal shift of the ferroelectric hysteresis loop) by exploiting the nanoscale interplay between chemistry, strain gradients, strain accommodation, and domain formation in compositionally-graded $PbZr_{1-x}Ti_xO_3$ (PZT) heterostructures. We find that variations in the nature of the compositional gradient and heterostructure thickness can be used to control both the crystal and domain structures giving rise to a nonintuitive evolution of the built-in potential which does not scale directly with the magnitude of the strain gradient as would be expected. Large built-in potentials are instead observed in compositionally-graded heterostructures that contain (1) compositional gradients that traverse chemistries associated with structural phase boundaries (such as the morphotropic phase boundary) and (2) ferroelastic domain structures. In turn, the built-in potential is observed to be dependent on a combination of flexoelectric effects (*i.e.*, polarization−strain gradient coupling), chemical-gradient effects (*i.e.*, polarization−chemical potential gradient coupling), local inhomogeneities

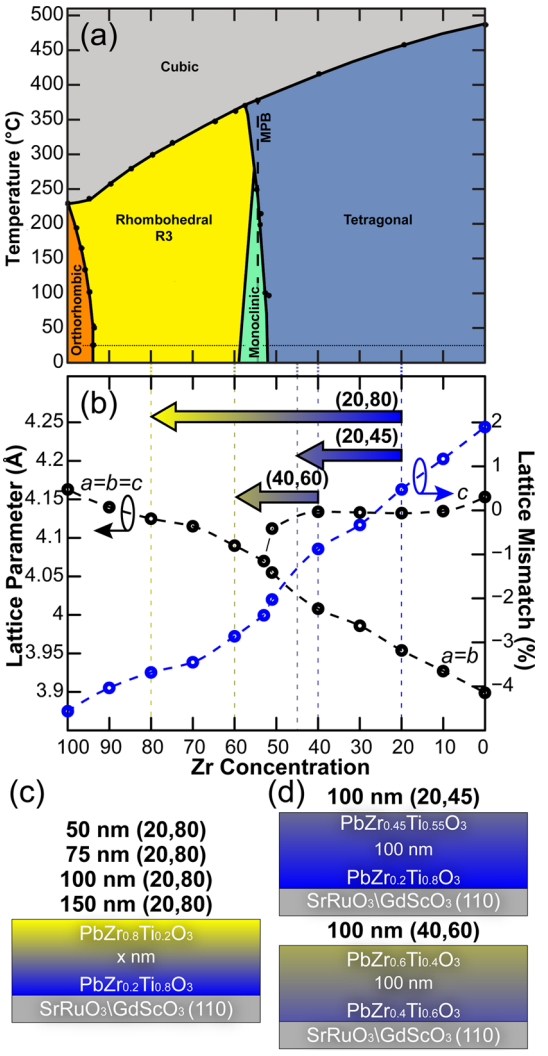

Figure 1. (a) $PbZr_{1-x}Ti_xO_3$ phase diagram, adapted from B. Jaffe *et al.*[41] (b) Bulk lattice parameter (shown in black) and calculated misfit strain (shown in blue) spanning across the $PbZr_{1-x}Ti_xO_3$ phase diagram. (c) Schematic illustrations of $PbZr_{0.8}Ti_{0.2}O_3$ ↔ $PbZr_{0.2}Ti_{0.8}O_3/SrRuO_3/GdScO_3$ (110) heterostructures: 50, 75, 100, and 150 nm thick. (d) Schematic illustrations of 100 nm thick $PbZr_yTi_{1-y}O_3$ ↔ $PbZr_xTi_{1-x}O_3/SrRuO_3/GdScO_3$ heterostructures spaning various compositional ranges (sample name: (*x*,*y*)).

(in structure or chemistry) that enhance strain (and/or chemical potential) gradients such as areas with nonlinear lattice parameter variation with chemistry or near ferroelastic domain boundaries. Regardless of origin, large built-in potentials act to suppress the dielectric permittivity, while having minimal impact on the magnitude of the polarization. Such observations are important to provide new routes to decouple ferroic susceptibilities and for the optimization of figures of merit for a range of nanoscale applications including piezoelectric-based vibrational energy harvesting[36−38] and pyroelectric-based thermal energy conversion.[6,39,40]

RESULTS AND DISCUSSION

Inspection of the composition−temperature phase diagram for the $PbZr_{1-x}Ti_xO_3$ system (Figure 1a)

reveals a structural competition between tetragonal and rhombohedral symmetry on the Ti- and Zr-rich sides, respectively. Likewise, the room-temperature lattice parameter-composition evolution (Figure 1b) reveals that the lattice parameters do not vary linearly with composition and instead change rapidly near the morphotropic phase boundary (MPB, $x = 0.48$).

On the basis of this information, we focused on compositionally-graded heterostructures $PbZr_{1-y}Ti_yO_3 \leftrightarrow PbZr_{1-x}Ti_xO_3$/30 nm $SrRuO_3/GdScO_3$ (110) (a = 5.45 Å, b = 5.75 Å, c = 7.93 Å, pseudocubic a_{pc} = 3.96 Å) grown using pulsed-laser deposition following previously established procedures (see details in the Methods section).[6,7] Growth on $GdScO_3$ substrates provides lattice mismatches between −4.6 to 2% as one transitions from $PbZrO_3$ to $PbTiO_3$ (Figure 1b, right axis). In all cases, the composition of the bottom-most $PbZr_{1-x}Ti_xO_3$ layer is chosen to be the composition with the least lattice mismatch to the substrate and all compositional gradients are controlled to be linear in nature. All heterostructures are named on the basis of the variation of the Zr-content upon transitioning from the substrate interface (x) to the free surface of the film (y) in the form (x,y).

In this work, we studied six compositionally-graded-heterostructure variants, which are separated into two groups for discussion. This first is a series probing the effects of film thickness variation wherein we probe 50, 75, 100, and 150 nm thick (20,80) compositionally-graded heterostructures (Figure 1c). These thicknesses were selected because they permit a large variation in the magnitude of the maximum theoretical average strain gradient (from 8.7×10^5 m^{-1} to 2.9×10^5 m^{-1} for the 50 and 150 nm thick heterostructures, respectively). Note that the theoretical strain gradients can be obtained by taking the difference in the misfit strain between the substrate and the bulk lattice parameter of the parent phases at the substrate−film interface and the free surface and dividing by the film thickness; values for lattice parameters are provided (Figure 1b). In addition, these variations in thickness also provide a pathway to alter the form and density of the ferroelastic domain structure.[42]

The second series of heterostructures probes the effects of varying the nature of the compositional gradient and focuses on 100 nm thick (20,45), (40,60), and (20,80) heterostructures (Figure 1d). This series of compositional gradients was selected for two reasons: (1) the (20,80) heterostructure (4.3×10^5 m^{-1}) has approximately double the strain gradient of the (20,45) (*i.e.*, 2.2×10^5 m^{-1}) and (40,60) (*i.e.*, 2.5×10^5 m^{-1}) heterostructures which allows us to probe the effect of varying strain gradient magnitude and (2) the (20,80) and (40,60) heterostructures include the MPB composition while the (20,45) heterostructure does not, allowing the role of the nonlinear lattice parameter evolution near the MPB in this system to be probed.

X-ray diffraction θ-2θ and reciprocal space mapping (RSM) studies found all heterostructure variants to be single-phase, fully epitaxial, and (001)-oriented regardless of thickness or gradient design (wide-angle, θ-2θ X-ray diffraction patterns are provided, Supporting Information, Figure S1). RSM studies were completed about the 103- and 332-diffraction conditions of the films and substrate, respectively (Figure 2). The positions of the bulk and strained peaks for the parent phases are provided for reference. Focusing on the thickness series of (20,80) heterostructures (Figure 2a−d), as expected the Q_y-values span continuously between the theoretical strained peak positions of the parent phases. As the thickness of the heterostructures increases, however, there is a slight increase in spectral weight toward lower Q_x-values and a slight decrease in spectral weight near the expected lattice parameter for strained $PbZr_{0.8}Ti_{0.2}O_3$. A quantitative measure of this relaxation can be obtained by comparing the logarithmically-scaled, weighted-mean intensity of the 103-diffraction condition to the theoretical strained and relaxed average peak positions (a description of the methodology used is provided, Supporting Information, Figure S2). From these analyses, both the 50 and 75 nm thick (20,80) heterostructures (Figure 2a,b) are found to be coherently strained to the substrate (within experimental resolution limits). As the thickness of the (20,80) heterostructure is increased to 100 nm (Figure 2c) and 150 nm (Figure 2d), the relaxation from the theoretical strained peak position increases to ∼10.6% and ∼22.3%, respectively. All told, these observations imply that strain relaxation increases with film thickness as would typically be expected.[43]

Similar analyses on the 100 nm thick compositionally-graded heterostructures with different gradient forms [*i.e.*, (20,45) (Figure 2e), (40,60) (Figure 2f), and (20,80) (Figure 2c)] again reveal that the Q_y-values span continuously between the theoretical strained-peak positions of the parent phases. Following the same procedure noted above, the (20,45) heterostructures are found to be coherently strained to the substrate (within the experimental resolution limits), but the (40,60) heterostructures exhibit partial strain relaxation (∼26.7% relaxed from the theoretical strained peak position). The minimal (or negligible) strain relaxation in the (20,45) heterostructures can be readily understood since the films possess uniform bulk tetragonal structure and smaller lattice parameter variation across the thickness of the heterostructure. On the other hand, the (40,60) heterostructures possess more than double the amount of strain relaxation than the (20,80) heterostructures despite having approximately half the theoretical strain gradient. This discrepancy can be understood by considering the lattice mismatch between the substrate and the bottom-layer $PbZr_{1-x}Ti_xO_3$, which in the (20,80) heterostructures is only 0.15% tensile as

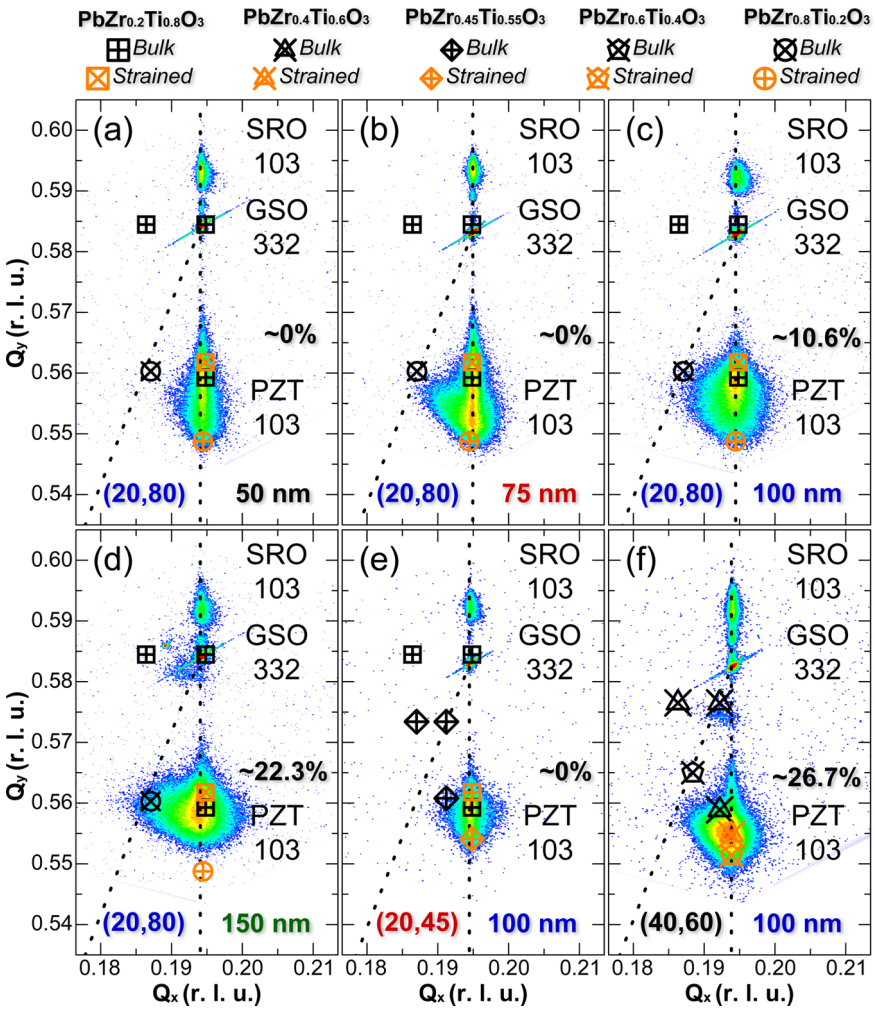

Figure 2. Reciprocal space mapping about the 103-diffraction conditions for $PbZr_yTi_{1-y}O_3$ ↔ $PbZr_xTi_{1-x}O_3/SrRuO_3/GdScO_3$ (110) heterostructures (sample name: (*x*,*y*)) (a) 50 nm (20,80), (b) 75 nm (20,80), (c) 100 nm (20,80), (d) 150 nm (20,80), (e) 100 nm (20,45), and (f) 100 nm (40,60). Dashed lines represent the coherently strain (vertical) and cubic (angled) lattice parameters and the expected peak positions for bulk (black) and strained (orange) versions of the parent phases are labeled in each graph. The percentage of strain relaxation is also noted.

compared to −1.2% compressive in the (40,60) heterostructures. Thus, the larger lattice mismatch at the substrate−film interface likely begets more pronounced and rapid strain relaxation.

The key insight from these analyses is that, regardless of the film thickness and the nature of the compositional gradient, the heterostructures retain a large majority (if not all) of the epitaxial strain imparted by the substrate. This stands in contrast to what is typically observed in homogeneous films of the various parent materials (100 nm thick $PbZr_{0.2}Ti_{0.8}O_3$, $PbZr_{0.52}Ti_{0.48}O_3$, and $PbZr_{0.8}Ti_{0.2}O_3$ heterostructures grown on $GdScO_3$ substrates reveal 0, 84.0, and 45.3% strain relaxation, respectively, Supporting Information, Figure S3). Thus, consistent with what has been observed in group IV and III−V semiconductor systems,[44,45] these results demonstrate that the presence of the compositional gradient (and in particular, those with minimal lattice mismatch at the film−substrate interface) provides a pathway to retain large residual strains and strain gradients not possible in homogeneous heterostructures.

Not only does changing the nature of the compositional gradient and heterostructure thickness impact the structure and strain state of the heterostructures, but it also can give rise to and vary both the density and nature of ferroelastic domains.[43,46] To image these nanoscale ferroelastic domains we conducted out-of-plane piezoresponse force microscopy (PFM) studies. Again, focusing first on the thickness series of (20,80) heterostructures, the 50 nm thick heterostructures are observed to exhibit a monodomain structure (Figure 3a), consistent with expectations for a (00l)-oriented, highly compressively strained tetragonal ferroelectric (such as Ti-rich $PbZr_{1-x}Ti_xO_3$). Upon increasing the thickness of the heterostructures to 75 and 100 nm, *c*/*a*/*c*/*a* domain structures (consisting of out-of-plane polarized *c* domains and in-plane polarized *a* domains) with density and domain width increasing with heterostructure thickness are observed (Figure 3b; data shown

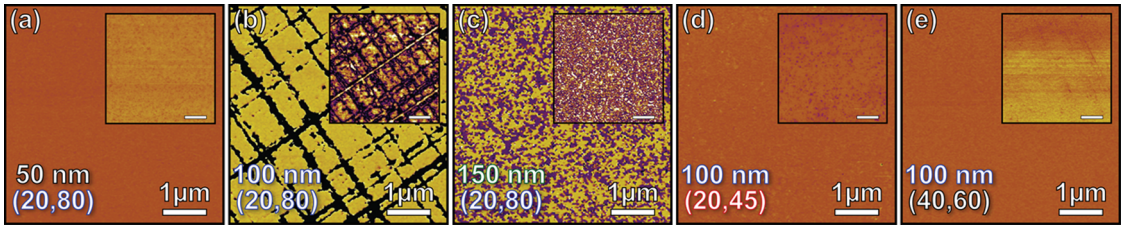

Figure 3. Vertical phase piezoresponse force microscopy images of $PbZr_{0.8}Ti_{0.2}O_3$ ↔ $PbZr_{0.2}Ti_{0.8}O_3$/$SrRuO_3$/$GdScO_3$ (110) heterostructures (sample name: (*x*,*y*)) (a) 50 nm (20,80), (b) 100 nm (20,80), (c) 150 nm (20,80), (d) 100 nm (20,45), and (e) 100 nm (40,60). A vertical amplitude piezoeresponse force microscopy image is provided as an inset in each of the figures.

only for the 100 nm heterostructure for brevity). Again, such a domain structure is typically observed only in tetragonal ferroelectrics (Supporting Information, Figure S4a).[43,47] Finally, for the 150 nm thick heterostructures, a complex mosaic-like domain structure is observed (Figure 3c), indicating that, at least at the surface, the tetragonal-like domain structure is no longer stabilized and instead the domain structure is consistent with typical rhombohedral $PbZr_{1-x}Ti_xO_3$ heterostructures (Supporting Information, Figure S4b). These observations can be understood by considering the driving forces for ferroelastic domain formation and the observed crystal structures. In the thinnest films, coherency is maintained and the large compressive strain drives the manifestation of a tetragonal-like crystal and monodomain structure. At intermediate thicknesses, the growing strain energy results in slight strain accommodation, but the residual epitaxial strain is enough still to stabilize the tetragonal crystal and domain structure. Finally, in the thickest heterostructures, more significant relaxation (especially at the free surface) results in loss of coherency to the substrate and relaxation (at least at the surface) to the parent rhombohedral phase (and domain structure).

We have also probed the effect of changing the nature of the compositional gradient on the domain structure evolution. PFM studies of both the 100 nm thick (20,45) (Figure 3d) and (40,60) (Figure 3f) heterostructures reveal a monodomain structure; once again, similar to, those observed in highly compressively strained tetragonal ferroelectrics. Such a monodomain structure in the (20,45) heterostructures is unsurprising, since the film is entirely on the tetragonal side of the phase diagram where compressive strains act to stabilize the *c* phase. Conversely, the presence of a monodomain structure in the (40,60) heterostructures is unexpected as these heterostructures have many attributes which should drive the formation of a polydomain structure. First, the (40,60) heterostructures have a considerably larger average misfit strain and subsequent relaxation (as compared to the (20,45) heterostructures). Second, they possess a large fraction of the heterostructure compositionally near the MPB where the flattened energy landscape between the structural variants facilitates ferroelastic domain formation[48] and nanodomain structures.[49,50] Third, the top ~50% of the film is compositionally such that it should have rhombohedral structure. Likely, the presence of the continually increasing compressive strain state, which transitions from −1.2% compressive at the film−substrate interface to −3.2% compressive at the free surface, enables the retention of considerably more strain than is achievable in homogeneous films, thereby stabilizing the tetragonal-like crystal and domain structure.

This understanding of how the nature of the compositional gradient and the heterostructure thickness can be manipulated to engineer the strain gradient and domain structure is important to obtain a comprehensive picture of how built-in potential and properties evolve in these heterostructures. To quantify the built-in potential, ferroelectric hysteresis loops were measured for the various heterostructures (for brevity, we show characteristic hysteresis loops measured at 1 kHz, Figure 4a,b, but loops at other frequencies are also provided, Supporting Information, Figure S5a−f). Similar to homogeneous ferroelectric thin films, all heterostructures studied here show large saturation and remanent polarization. Unlike homogeneous ferroelectric thin films, in compositionally-graded heterostructures the large strain gradients and variations in the chemical composition can generate built-in potentials[7,8,22,51,52] which can be quantified by the horizontal shift of the ferroelectric hysteresis loop along the voltage (or field) axis (*i.e.*, the difference between the coercive field). Note that these built-in potentials are innate to the compositionally-graded materials (in its current strain state) and care was taken to exclude additional effects that can give rise to shifts by using symmetric, perovskite-based, epitaxial $SrRuO_3$ top and bottom electrodes.[53]

On the basis of common understanding of flexoelectric effects and built-in potentials,[7,17,18,27,54] one would empirically expect that the magnitude of the built-in potential would be primarily governed by the magnitude of the strain gradient. Thus, for the thickness series of (20,80) heterostructures (Figure 4a), the magnitude of the built-in potential should be inversely proportional to the thickness. The actual results, however, do not follow this trend, and instead, the built-in potential is found to increase with film thickness until falling dramatically in the case of the 150 nm thick heterostructures. The measured built-in potential was found to be 0.380 ± 0.045 V (76 ± 9 kV/cm), 0.833 ± 0.038 V (111 ± 5 kV/cm),

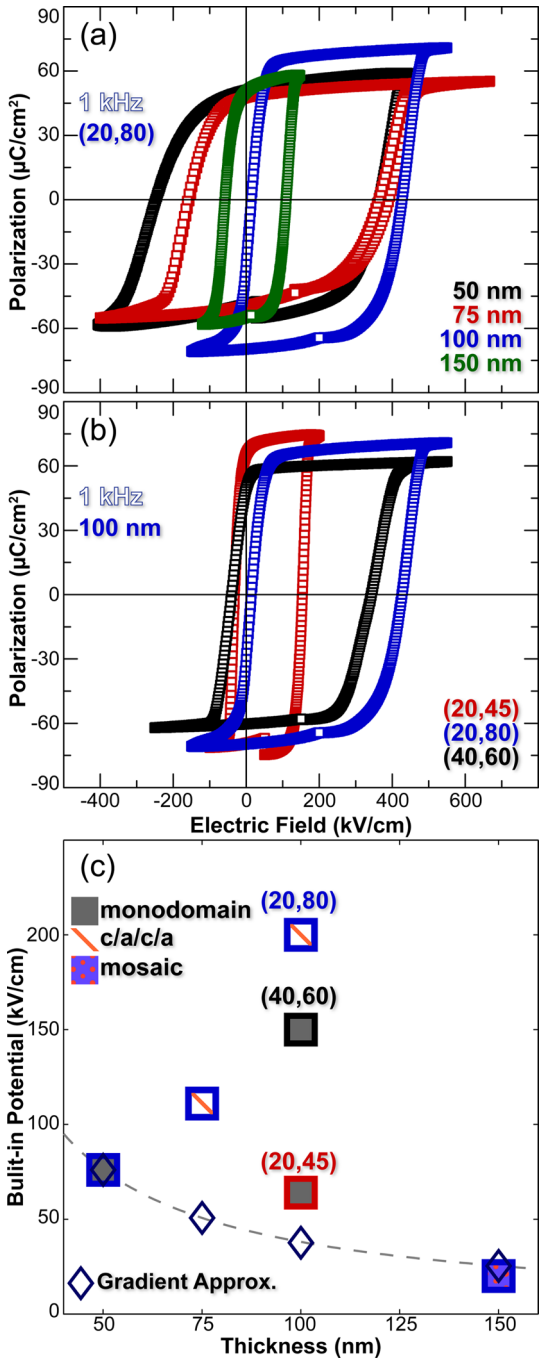

Figure 4. Room temperature polarization−electric field hysteresis loops of $PbZr_yTi_{1-y}O_3$ ↔ $PbZr_xTi_{1-x}O_3/SrRuO_3/GdScO_3$ heterostructures (sample name: (*x*,*y*)) measured at 1 kHz of various (a) (20,80) heterostructure thicknesses and (b) various 100 nm thick compositional-gradient designs. (c) Plot of measured built-in potential as a function of film thickness for all compositionally-graded heterostructures studied. Dashed line and small diamond markers represents an estimation of the built-in potentials based on the flexo-chemo-electric coefficient of the 50 nm (20,80) heterostructures.

2.00 ± 0.090 V (200 ± 9 kV/cm), and 0.4 ± 0.020 V (20 ± 1 kV/cm) for the 50, 75, 100, and 150 nm thick (20,80) heterostructures, respectively.

Only by returning to the differences in the crystal and domain structure can this trend be explained. Overall, as the thickness of the film increases the maximum average theoretical strain gradient and residual strain decreases, and therefore, (under the assumption that the built-in potential is primarily governed by the strain gradient) the built-in potential should monotonically decrease with thickness. In turn, this suggests that additional contributions to the built-in potential must be present. To shed more light on this concept, we can establish a frame of reference for the "intrinsic" strain- and composition-gradient contribution to the built-in potential by first considering the 50 nm thick (20,80) heterostructures. These heterostructures, which are coherently strained and monodomain, possess a structure most closely matched with the "ideal" compositionally- and strain-graded heterostructure concept. Following the methods used in the community,[51] we can extract a coefficient of the same form and units as the flexoelectric coefficient, which we here call the *effective flexo-chemo-electric coefficient*, to acknowledge the inclusion of additional contributions, such as chemical-gradient effects, which are not traditionally considered in the flexoelectric coefficient. Knowing that the strain gradient is 8.7×10^5 m^{-1} and that the built in potential is 0.38 V, we calculate the effective flexo-chemo-electric coefficient to be $|\mu_{eff}|$ = 12 nC/m (see Supporting Information for details). This value lies directly in-between experimentally reported flexoelectric coefficients for the $PbZr_{1-x}Ti_xO_3$ system (500−2,000 nC/m, measured *via* bending of chemically homogeneous samples)[18,23,51] and first-principles calculations (which include only strain-gradient-based flexoelectric effects; for $PbTiO_3$ μ = 0.165 nC/m).[26−28] This comparison brings up a number of interesting points. First, as is typical, our experimental measures of these effects return values much larger than the first-principles predictions suggesting that additional contributions to these effects could be present. Second, our experimental values are considerably smaller than most experimental values, which might suggest that the chemical-gradient effect could be of the opposite sign to that of the classic strain-gradient effects.

Using this effective flexo-chemo-electric coefficient, we can then make a simple prediction of how the built-in potential should scale with thickness (dashed line, Figure 4c); since the maximum theoretical strain gradient is inversely proportional to the heterostructure thickness the built-in potential should fall of with increasing thickness. What is clear, however, is that the built-in potentials measured for the 75 and 100 nm thick (20,80) heterostructures variants are greatly enhanced compared to this expected trend. To explain this unexpected observation requires consideration of the strain state and domain structure of the heterostructures. Both the 75 and 100 nm thick (20,80) heterostructures exhibit a *c*/*a*/*c*/*a* domain structure where the size and density of the *a* domains increases with thickness, matching the observed trend in the

built-in potential. This implies that the formation of ferroelastic domains could be responsible for the larger built-in potential. We hypothesize that the presence of ferroelastic *a* domains, and the corresponding rotation of the polarization direction at such domain boundaries, gives rise to large, localized strain gradients[16,31] and fields[31,32] that contribute to the built-in potential. Since the largest built-in potential is observed in the 100 nm thick (20,80) heterostructures despite the significant reduction in strain gradient, this suggests that the *c*/*a*/*c*/*a* domain structures are key in defining the evolution of these effects. Finally, in the 150 nm thick heterostructures, which possess the most severe strain relaxation and domain structures indicative of complete or near-complete relaxation at the surface of the film, the relaxation must be severe enough to reduce the overall magnitude of the strain gradient in the film thereby reducing the overall built-in potential.

A similar analysis of the built-in potentials for the 100 nm thick (20,45), (40,60), and (20,80) heterostructures (Figure 4b), where the built-in potentials were measured to be 0.64 ± 0.03 V (64 ± 3 kV/cm), 1.5 ± 0.09 V (150 ± 9 kV/cm), and 2.0 ± 0.09 V (200 ± 9 kV/cm), respectively, can be completed. Recall that the theoretical strain gradients for the (20,45) and (40,60) heterostructures are approximately half of that of the (20,80) heterostructures and that both heterostructures exhibit a monodomain structure. Beginning with the (40,60) heterostructures, the lattice parameters defining the strain gradient increase rapidly, in a nonlinear fashion, upon transitioning through the MPB composition,[55] we hypothesize that the presence of locally enhanced strain gradients within the film associated with the MPB compositions could greatly increase the magnitude of the macroscopic built-in potential, even in the absence of domain structures. It should be noted, that heterostructures encompassing the MPB could also exhibit enhanced built-in potentials because of a local variation in the magnitude of the flexoelectric coefficient, which is typically larger near the MPB.[27,56] Additionally, the fact that the built-in potential of the (40,60) heterostructures are larger than that of the 50 nm thick (20,80) heterostructures suggests that the chemical-potential-gradient effects are likely smaller (because of the reduced compositional range) and are still of the opposite sign of the strain-gradient effects, pointing to a dependence similar to that for the strain-gradient effects on the composition range and thickness for the compositional-gradient effects. On the other hand, in the (20,45) heterostructures the reduced built-in potential is like the result of the fact that the composition range probed exists entirely in the tetragonal phase region of the $PbZr_{1-x}Ti_xO_3$ phase diagram and that the lattice parameters increase smoothly with increasing Zr content thereby excluding any locally enhanced strain gradients in the films. Additionally, the chemical-gradient effects in the (20,45) heterostructures should also be relatively smaller in magnitude (compared to the 50 nm thick (20,80) heterostructures), but again we cannot fully decouple the effects in a manner that allow us to quantify the magnitude of this chemical-gradient effect uniquely. All told, the ultimate manifestation of built-in potential in the compositionally-graded heterostructures varies in a rather complex and, at times, unintuitive manner as a function of film thickness, lattice parameter variation, domain formation, strain relaxation, compositional end members, and much more. Overall, the built-in potentials are larger when locally enhanced strain gradients exist such as occur upon transitioning through the MPB composition and at/near ferroelastic domain boundaries. These observations suggest that the macroscopic manifestation of built-in potential includes aspects of flexoelectric effects (*i.e.*, polarization−strain gradient coupling), chemical-gradient effects (*i.e.*, polarization−chemical potential gradient coupling), and local inhomogeneities that enhance strain (and/or chemical) gradients which occur in areas with rapid lattice parameter evolution like near the MPB composition or near ferroelastic domain boundaries.

From a materials design perspective, however, we care about the nature of and how to control the built-in potential of these heterostructures because it can have profound effects on the nature of material properties. Prior studies of compositionally-graded $PbZr_{1-x}Ti_xO_3$ heterostructures suggest that the presence of built-in potentials can reduce the dielectric permittivity[10,57] by acting to stiffen both intrinsic (*i.e.*, with the bulk of a domain) and extrinsic (*i.e.*, from motion of domain walls) responses to excitation under application of small ac fields. Reducing the permittivity is key to optimizing these materials for advanced nanoscale applications where the figure of merit for both electromechanical[58−60] ($k^2 = e^2/c\varepsilon_r\varepsilon_0$, where e is the direct-effect piezoelectric coefficient and c is the material stiffness, ε_r is the dielectric permittivity, and ε_0 is the permittivity of free space) and thermal[59,61,62] ($k^2 = \pi^2 T/C_p\varepsilon_r\varepsilon_0$, where π is the pyroelectric coefficient, T is the temperature of operation, and C_p is the heat capacity) devices is defined by so-called coupling factors. Routes to tune material stiffness, heat capacity, *etc.* are limited and thus the ability to tune these figures of merit is confined to routes that decouple the piezoelectric or pyroelectric coefficients from the permittivity.

To quantify the combined influence of the crystal and domain structure and built-in potential on the susceptibility, the low-field dielectric permittivity was measured as a function of frequency for all heterostructures (for brevity, we show characteristic permittivity measurements at an ac excitation of 8 mV from 1 to 100 kHz). Again, we begin by exploring the thickness series of (20,80) heterostructures (Figure 5a; dielectric loss is provided in the Supporting Information, Figure S6) where the dielectric permittivity was found to be 71.8, 68.5, 86.2, and 158.2 (at 10 kHz) for 50,

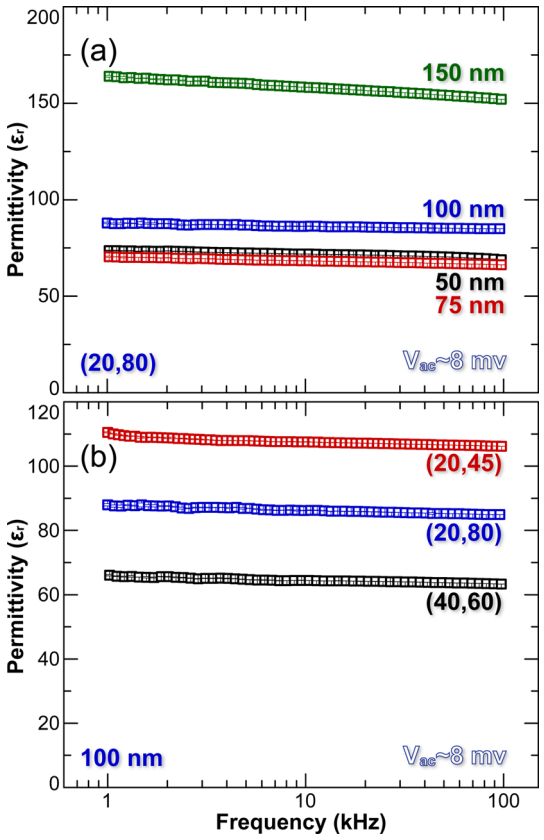

Figure 5. Room temperature dielectric permittivity (measured at V_{ac} = 8 mV, error <7%) as a function of frequency for $PbZr_yTi_{1-y}O_3$ ↔ $PbZr_xTi_{1-x}O_3/SrRuO_3/GdScO_3$ compositionally-graded heterostructures (sample name: (*x*,*y*)) for various (a) (20,80) heterostructure thicknesses and (b) various 100 nm thick compositional-gradient designs.

75, 100, and 150 nm thick heterostructures, respectively. Beginning with the 50 nm thick heterostructures (which are monodomain, with a built-in potential of 76 ± 9 kV/cm) the permittivity is suppressed to a value lower than that previously reported for intrinsic permittivity (~90) for monodomain, homogeneous $PbZr_{0.2}Ti_{0.8}O_3$ thin films.[63] This observation is readily understood since there are no extrinsic contributions (since there are no domain walls) combined with the sizable built-in potential, which serves to reduce the intrinsic susceptibility and thus the overall response. As the heterostructure thickness increases, domain structures emerge that influence the permittivity in competing ways. The presence of ferroelastic domains is known to give rise to extrinsic contributions to the dielectric permittivity, which typically enhance the dielectric permittivity,[64−66] and this work has shown that their formation also corresponds to an increases the magnitude of the built-in potential, which should work to suppress both the intrinsic and extrinsic contributions. Thus, in the 75 nm thick heterostructures (where there is a small density of domains and a larger built-in field (111 ± 5 kV/cm), the combination manifests as a similar dielectric permittivity to the 50 nm thick heterostructures (within the error of measurement). By the time the thickness reaches 100 nm, however, the presence of a robust and denser domain structure and the associated extrinsic contributions to the dielectric permittivity overcomes the effects of the built-in field (200 ± 9 kV/cm), causing a slight increase in permittivity (although it is still smaller than that reported for monodomain, homogeneous $PbZr_{0.2}Ti_{0.8}O_3$ films). Finally, in the 150 nm thick heterostructures, which have complex, mosaic-like domain structures, with the smallest built-in potential of 20 ± 1 kV/cm, the largest permittivity is observed; a result of the minimally suppressed intrinsic and extrinsic contributions to permittivity.

Using a similar approach, we can also understand the evolution of the permittivity in the 100 nm thick (20,45), (40,60), and (20,80) heterostructures (Figure 5b). In this set of heterostructures, the (20,45) variants have the largest permittivity (~107.5 at 10 kHz) and the (40,60) heterostructures have the lowest permittivity (~64.4 at 10 kHz). Again, we can rationalize these trends through the combination of the crystal and domain structure and built-in potential evolution. First, for the (20,45) heterostructures (with monodomain structure and a built-in potential of 64 ± 3 kV/cm), the measured permittivity is close to the expected permittivity for a monodomain, homogeneous $PbZr_{0.2}Ti_{0.8}O_3$ thin film,[63] indicating that the dielectric response is dominated by the intrinsic response of the monodomain structure, and that the small built-in potential does not significantly influence the dielectric response. For the (40,60) heterostructures (with monodomain structure and sizable built-in potential of 150 ± 9 kV/cm), the larger built-in potential greatly reduces the intrinsic permittivity, and since there are no domain walls, there is no extrinsic contribution resulting in the lowest observed dielectric response. We note that to the best of our knowledge, that these are the lowest permittivity values reported for any $PbZr_{1-x}Ti_xO_3$ thin film system to date. Progressing to the (20,80) heterostructures, *c*/*a*/*c*/*a* domain structures are formed generating an extrinsic response, which enhances the permittivity more than the increase in built-in potential can suppress it, causing a slight increase in permittivity compared to the 100 nm thick (40,60) heterostructures. Regardless, the observation of the lowest reported room temperature dielectric permittivity for the $PbZr_{1-x}Ti_xO_3$ system, measured in the (40,60) heterostructures, which are compositionally close to the MPB (where a maximum in dielectric permittivity should be expected) demonstrates the efficacy of compositional-gradients in generating built-in potentials, which can provide routes to strongly decouple the ferroic and dielectric responses.

Altogether, through judicious exploration of a range of nanoscale controlled, compositionally-graded heterostructures, we have demonstrated that the ferroelectric and dielectric response is highly influenced by the crystal and domain structure which can be manipulated by the heterostructure design. Specifically,

we show that the magnitude of the built-in potential is only minimally influenced by the magnitude of the average strain gradient and instead is determined a combination of flexoelectric effects (*i.e.*, polarization−strain gradient coupling), chemical-gradient effects (*i.e.*, polarization−chemical potential gradient coupling), and local inhomogeneities that enhance strain (and/or chemical) gradients such as areas with rapid lattice parameter evolution like that near the MPB composition or near ferroelastic domain boundaries. This work highlights the importance of local nanoscale strain gradients in generating large macroscopic built-in potentials, yielding new perspectives on how to design ferroelectric thin films to maximize built-in potentials while having minimal effect on the ferroic responses. In turn, these results provide a facile route to independently tune susceptibilities in ferroelectric thin films essential for optimizing materials figure of merit for a range of nanoscale applications.

CONCLUSIONS

In summary, we have explored how deterministic control of compositionally-graded heterostructure form (in terms of the nature of the compositional gradient and heterostructure thickness) can be used to tune the crystal and domain structure and what the influence of these changes are for the evolution of built-in potentials, ferroelectric, and dielectric response in $PbZr_{1-x}Ti_xO_3$ thin films. The magnitude of the built-in potential is found not to scale directly with the magnitude of the strain gradient (as would be expected), but instead, large built-in potentials are observed in the compositionally-graded heterostructures, which contain locally enhanced strain gradients that occur when traversing chemistries associated with structural phase boundaries where there are abrupt changes in material lattice parameter and at/near ferroelastic domain boundaries. These observations suggest that the built-in potential observed in these materials is likely a manifestation of a combination of flexoelectric effects (*i.e.*, polarization−strain gradient coupling), chemical-gradient effects (*i.e.*, polarization−chemical potential gradient coupling), and local inhomogeneities that enhance strain (and/or chemical) gradients. Regardless of origin, large built-in potentials act to suppress the dielectric permittivity while having minimal impact on the magnitude of the polarization, providing a facile route to optimize these materials for a range of nanoapplications from vibrational energy harvesting to thermal energy conversion and beyond.

METHODS

Film Growth. Compositionally-graded heterostructures of $PbZr_{1-x}Ti_xO_3$ (PZT)/30 nm $SrRuO_3$/$GdScO_3$ (110) were grown using pulsed-laser deposition from $Pb_{1.1}Zr_{0.2}Ti_{0.8}O_3$ and $Pb_{1.1}Zr_{0.8}Ti_{0.2}O_3$ targets.[7] The bottom electrode $SrRuO_3$ films were grown at 630 °C in an oxygen pressure of 100 mTorr at a laser fluence 1.8 J/cm^2 and a frequency of 13 Hz. The compositionally-graded PZT layers were grown at 600 °C in an oxygen pressure of 200 mTorr, during the growth the laser fluence was maintained at 1.9 J/cm^2, pulsed at a frequency of 3 Hz. The composition of the compositionally-graded layers was controlled by continuously varying the composition from $PbZr_xTi_{1-x}O_3$ to $PbZr_yTi_{1-y}O_3$ using a programmable target rotator (Neocera, LLC) that was synced with the excimer laser. For all the samples, films were cooled in an oxygen pressure of 700 Torr. Symmetric capacitor structures were fabricated by subsequent deposition of 80 nm $SrRuO_3$ top electrodes defined using a MgO hard-mask process.[67]

Crystal Structure and Ferroelectric Domain Structure Analysis. The structure of these heterostructures was studied using X-ray diffraction reciprocal space mapping (RSM) about the 103- and 332-diffraction conditions for the film and substrate, respectively. We utilize the Four-circle High Resolution X-ray Diffractometer (PANALYTICAL X'PERT PRO). Detail ferroelectric domain analyses of the films were carried out using Piezoresponse Force Microscopy (Cypher, Asylum research).

Dielectric and Ferroelectric Properties. The dielectric permittivity was extracted from the measured capacitance (C) using $C = ((\varepsilon_0\varepsilon_r A)/d)$ where A is the area of the capacitor and d is the thickness of the film. Prior to measurement, the films were poled with a negative bias for 0.1 ms and films were measured at remanence. The dielectric permittivity as a function of frequency was measured with an ac excitation voltage of 8 mV (rms). Rayliegh studies confirmed that the ac excitation was small enough to preclude irreversible domain wall motion. Ferroelectric hysteresis loops were measured using a Radiant Multiferroics Tester as a function of frequency from 0.1−20 kHz.

Conflict of Interest: The authors declare no competing financial interest.

Acknowledgment. J.C.A. and L.W.M. acknowledge support from the National Science Foundation under grant number DMR-1451219. A.R.D. and S.P. acknowledge the support of the Army Research Office under grant number W911NF-14-1-0104. R.V.K.M. acknowledges support from the National Science Foundation under grant ENG-1434147.

Supporting Information Available: Additional X-ray diffraction studies, determination of residual strain in compositionally-graded heterostructures, additionally reciprocal space mapping studies, additional piezoresponse force microscopy studies, additional ferroelectric hysteresis loops and dielectric loss measurements. The Supporting Information is available free of charge on the ACS Publications website at DOI: 10.1021/acsnano.5b02289.

REFERENCES AND NOTES

1. Baek, S. H.; Park, J.; Kim, D. M.; Aksyuk, V. A.; Das, R. R.; Bu, S. D.; Felker, D. A.; Lettieri, J.; Vaithyanathan, V.; Bharadwaja, S. S. N.; *et al.* Giant Piezoelectricity on Si for Hyperactive MEMS. *Science* **2011**, *334*, 958–961.
2. Scott, J. F. Applications of Modern Ferroelectrics. *Science* **2007**, *315*, 954–959.
3. Setter, N.; Damjanovic, D.; Eng, L.; Fox, G.; Gevorgian, S.; Hong, S.; Kingon, A.; Kohlstedt, H.; Park, N. Y.; Stephenson, G. B.; *et al.* Ferroelectric Thin Films: Review of Materials, Properties, and Applications. *J. Appl. Phys.* **2006**, *100*, 051606–051606−46.
4. Dawber, M.; Rabe, K. M.; Scott, J. F. Physics of Thin-Film Ferroelectric Oxides. *Rev. Mod. Phys.* **2005**, *77*, 1083–1130.
5. Schlom, D. G.; Chen, L.; Eom, C.; Rabe, K. M.; Streiffer, S. K.; Triscone, J. Strain Tuning of Ferroelectric Thin Films. *Annu. Rev. Mater. Res.* **2007**, *37*, 589–626.

6. Mangalam, R. V. K.; Agar, J. C.; Damodaran, A. R.; Karthik, J.; Martin, L. W. Improved Pyroelectric Figures of Merit in Compositionally Graded $PbZr_{1-x}Ti_xO_3$ Thin Films. *ACS Appl. Mater. Interfaces* **2013**, *5*, 13235–13241.
7. Mangalam, R. V. K.; Karthik, J.; Damodaran, A. R.; Agar, J. C.; Martin, L. W. Unexpected Crystal and Domain Structures and Properties in Compositionally Graded $PbZr_{1-x}Ti_xO_3$ Thin Films. *Adv. Mater.* **2013**, *25*, 1761–1767.
8. Lee, D.; Yang, S. M.; Yoon, J.; Noh, T. W. Flexoelectric Rectification of Charge Transport in Strain-Graded Dielectrics. *Nano Lett.* **2012**, *12*, 6436–6440.
9. Lee, D.; Yoon, A.; Jang, S. Y.; Yoon, J. G.; Chung, J. S.; Kim, M.; Scott, J. F.; Noh, T. W. Giant Flexoelectric Effect in Ferroelectric Epitaxial Thin Films. *Phys. Rev. Lett.* **2011**, *107*, 057602–057602−4.
10. Catalan, G.; Sinnamon, L. J.; Gregg, J. M. The Effect of Flexoelectricity on the Dielectric Properties of Inhomogeneously Strained Ferroelectric Thin Films. *J. Phys.: Condens. Matter* **2004**, *16*, 2253–2264.
11. Catalan, G.; Noheda, B.; McAneney, J.; Sinnamon, L. J.; Gregg, J. M. Strain Gradients in Epitaxial Ferroelectrics. *Phys. Rev. B: Condens. Matter Mater. Phys.* **2005**, *72*, 020102–020102−4.
12. Gruverman, A.; Rodriguez, B. J.; Kingon, A. I.; Nemanich, R. J.; Tagantsev, A. K.; Cross, J. S.; Tsukada, M. Mechanical Stress Effect on Imprint Behavior of Integrated Ferroelectric Capacitors. *Appl. Phys. Lett.* **2003**, *83*, 728–730.
13. Wen, Z.; Qiu, X.; Li, C.; Zheng, C.; Ge, X.; Li, A.; Wu, D. Mechanical Switching of Ferroelectric Polarization in Ultrathin $BaTiO_3$ Films: The Effects of Epitaxial Strain. *Appl. Phys. Lett.* **2014**, *104*, 042907–5.
14. Lu, H.; Bark, C. W.; Esque de los Ojos, D.; Alcala, J.; Eom, C. B.; Catalan, G.; Gruverman, A. Mechanical Writing of Ferroelectric Polarization. *Science* **2012**, *336*, 59–61.
15. Lee, D.; Jeon, B. C.; Yoon, A.; Shin, Y. J.; Lee, M. H.; Song, T. K.; Bu, S. D.; Kim, M.; Chung, J.; Yoon, J.; Noh, T. W. Flexoelectric Control of Defect Formation in Ferroelectric Epitaxial Thin Films. *Adv. Mater.* **2014**, *26*, 5005–5011.
16. Catalan, G.; Lubk, A.; Vlooswijk, A. H. G.; Snoeck, E.; Magen, C.; Janssens, A.; Rispens, G.; Rijnders, G.; Blank, D. H. A.; Noheda, B. Flexoelectric Rotation of Polarization in Ferroelectric Thin Films. *Nat. Mater.* **2011**, *10*, 963–967.
17. Yudin, P.; Tagantsev, A. Fundamentals of Flexoelectricity in Solids. *Nanotechnology* **2013**, *24*, 432001–432036.
18. Zubko, P.; Catalan, G.; Tagantsev, A. K. Flexoelectric Effect in Solids. *Annu. Rev. Mater. Res.* **2013**, *43*, 387–421.
19. Mantese, J. V.; Schubring, N. W.; Micheli, A. L.; Catalan, A. B. Ferroelectric Thin Films with Polarization Gradients Normal to the Growth Surface. *Appl. Phys. Lett.* **1995**, *67*, 721–723.
20. Mantese, J. V.; Schubring, N. W.; Micheli, A. L.; Catalan, A. B.; Mohammed, M. S.; Naik, R.; Auner, G. W. Slater Model Applied to Polarization Graded Ferroelectrics. *Appl. Phys. Lett.* **1997**, *71*, 2047–2049.
21. Brazier, M.; McElfresh, M.; Mansour, S. Unconventional Hysteresis Behavior in Compositionally Graded $Pb(Zr,Ti)O_3$ Thin Films. *Appl. Phys. Lett.* **1998**, *72*, 1121–1123.
22. Cross, L. E. Flexoelectric Effects: Charge Separation in Insulating Solids Subjected to Elastic Strain Gradients. *J. Mater. Sci.* **2006**, *41*, 53–63.
23. Ma, W.; Cross, L. E. Strain-Gradient-Induced Electric Polarization in Lead Zirconate Titanate Ceramics. *Appl. Phys. Lett.* **2003**, *82*, 3293–3295.
24. Chu, B.; Zhu, W.; Li, N.; Cross, L. E. Flexure Mode Flexoelectric Piezoelectric Composites. *J. Appl. Phys.* **2009**, *106*, 104109–104109−3.
25. Fu, J. Y.; Zhu, W.; Li, N.; Smith, N. B.; Cross, L. E. Gradient Scaling Phenomenon in Microsize Flexoelectric Piezoelectric Composites. *Appl. Phys. Lett.* **2007**, *91*, 182910–182910−3.
26. Hong, J.; Vanderbilt, D. First-Principles Theory and Calculation of Flexoelectricity. *Phys. Rev. B: Condens. Matter Mater. Phys.* **2013**, *88*, 174107–174107−24.
27. Tagantsev, A. K. Piezoelectricity and Flexoelectricity in Crystalline Dielectrics. *Phys. Rev. B: Condens. Matter Mater. Phys.* **1986**, *34*, 5883–5889.
28. Ponomareva, I.; Tagantsev, A.; Bellaiche, L. Finite-Temperature Flexoelectricity in Ferroelectric Thin Films from First Principles. *Phys. Rev. B: Condens. Matter Mater. Phys.* **2012**, *85*, 104101–104101−5.
29. Biancoli, A.; Fancher, C. M.; Jones, J. L.; Damjanovic, D. Breaking of Macroscopic Centric Symmetry in Paraelectric Phases of Ferroelectric Materials and Implications for Flexoelectricity. *Nat. Mater.* **2014**, *14*, 224–229.
30. Brazier, M.; McElfresh, M.; Mansour, S. Origin of Anomalous Polarization Offsets in Compositionally Graded $Pb(Zr, Ti)O_3$ Thin Films. *Appl. Phys. Lett.* **1999**, *74*, 299–301.
31. Gao, P.; Britson, J.; Nelson, C. T.; Jokisaari, J. R.; Duan, C.; Trassin, M.; Baek, S.; Guo, H.; Li, L.; Wang, Y.; *et al.* Ferroelastic Domain Switching Dynamics Under Electrical and Mechanical Excitations. *Nat. Commun.* **2014**, *5*, 3801–3801−8.
32. Britson, J.; Nelson, C.; Pan, X.; Chen, L. First-Order Morphological Transition of Ferroelastic Domains in Ferroelectric Thin Films. *Acta Mater.* **2014**, *75*, 188–197.
33. Zhang, J.; Xu, R.; Damodaran, A. R.; Chen, Z. H.; Martin, L. W. Understanding Order in Compositionally Graded Ferroelectrics: Flexoelectricity, Gradient, and Depolarization Field Effects. *Phys. Rev. B: Condens. Matter Mater. Phys.* **2014**, *89*, 224101–224101−11.
34. Tagantsev, A. K.; Yurkov, A. S. Flexoelectric Effect in Finite Samples. *J. Appl. Phys.* **2012**, *112*, 044103–044103−7.
35. Stengel, M. Microscopic Response to Inhomogeneous Deformations in Curvilinear Coordinates. *Nat. Commun.* **2013**, *4*, 2693–2693−8.
36. Qin, Y.; Wang, X.; Wang, Z. L. Microfibre-Nanowire Hybrid Structure for Energy Scavenging. *Nature* **2008**, *451*, 809–U5.
37. Trolier-McKinstry, S.; Griggio, F.; Yaeger, C.; Jousse, P.; Zhao, D.; Bharadwaja, S. S. N.; Jackson, T. N.; Jesse, S.; Kalinin, S. V.; Wasa, K. Designing Piezoelectric Films for Micro Electromechanical Systems. *IEEE Trans. Ultrason. Ferroelectr. Freq. Control* **2011**, *58*, 1782–1792.
38. Wang, Z. L.; Song, J. Piezoelectric Nanogenerators Based on Zinc Oxide Nanowire Arrays. *Science* **2006**, *312*, 242–246.
39. Yang, Y.; Guo, W.; Pradel, K. C.; Zhu, G.; Zhou, Y.; Zhang, Y.; Hu, Y.; Lin, L.; Wang, Z. L. Pyroelectric Nanogenerators for Harvesting Thermoelectric Energy. *Nano Lett.* **2012**, *12*, 2833–2838.
40. Jin, F.; Auner, G. W.; Naik, R.; Schubring, N. W.; Mantese, J. V.; Catalan, A. B.; Micheli, A. L. Giant Effective Pyroelectric Coefficients from Graded Ferroelectric Devices. *Appl. Phys. Lett.* **1998**, *73*, 2838–2840.
41. Jaffe, B.; Roth, R.; Marzullo, S. Piezoelectric Properties of Lead Zirconate-Lead Titanate Solid-Solution Ceramics. *J. Appl. Phys.* **1954**, *25*, 809–810.
42. Pertsev, N.; Zembilgotov, A. Energetics and Geometry of 90° domain Structures in Epitaxial Ferroelectric and Ferroelastic Films. *J. Appl. Phys.* **1995**, *78*, 6170–6180.
43. Speck, J. S.; Pompe, W. Domain Configurations due to Multiple Misfit Relaxation Mechanisms in Epitaxial Ferroelectric Thin Films. I. Theory. *J. Appl. Phys.* **1994**, *76*, 466–476.
44. Bertoli, B.; Suarez, E. N.; Ayers, J. E.; Jain, F. C. Misfit Dislocation Density and Strain Relaxation in Graded Semiconductor Heterostructures with Arbitrary Composition Profiles. *J. Appl. Phys.* **2009**, *106*, 073519–073526.
45. Romanato, F.; Napolitani, E.; Carnera, A.; Drigo, A. V.; Lazzarini, L.; Salviati, G.; Ferrari, C.; Bosacchi, A.; Franchi, S. Strain Relaxation in Graded Composition $InxGa_{1-x}As$/GaAs Buffer Layers. *J. Appl. Phys.* **1999**, *86*, 4748–4755.
46. Speck, J. S.; Seifert, A.; Pompe, W.; Ramesh, R. Domain Configurations due to Multiple Misfit Relaxation Mechanisms in Epitaxial Ferroelectric Thin Films. II. Experimental Verification and Implications. *J. Appl. Phys.* **1994**, *76*, 477–483.
47. Karthik, J.; Agar, J. C.; Damodaran, A. R.; Martin, L. W. Effect of 90° Domain Walls and Thermal Expansion Mismatch on the Pyroelectric Properties of Epitaxial $PbZr_{0.2}Ti_{0.8}O_3$ Thin Films. *Phys. Rev. Lett.* **2012**, *109*, 257602–257602−5.

48. Damjanovic, D. Contributions to the Piezoelectric Effect in Ferroelectric Single Crystals and Ceramics. *J. Am. Ceram. Soc.* **2005**, *88*, 2663–2676.
49. Theissmann, R.; Schmitt, L. A.; Kling, J.; Schierholz, R.; Schonau, K. A.; Fuess, H.; Knapp, M.; Kungl, H.; Hoffmann, M. J. Nanodomains in Morphotropic Lead Zirconate Titanate Ceramics: On the Origin of the Strong Piezoelectric Effect. *J. Appl. Phys.* **2007**, *102*, 024111–024117.
50. Agar, J. C.; Mangalam, R. V. K.; Damodaran, A. R.; Velarde, G.; Karthik, J.; Okatan, M. B.; Chen, Z. H.; Jesse, S.; Balke, N.; Kalinin, S. V.; *et al.* Tuning Susceptibility *via* Misfit Strain in Relaxed Morphotropic Phase Boundary $PbZr_{1-X}Ti_xO_3$ Epitaxial Thin Films. *Adv. Mater. Interfaces* **2014**, *1*, 1400098–1400098−8.
51. Ma, W. A Study of Flexoelectric Coupling Associated Internal Electric Field and Stress in Thin Film Ferroelectrics. *Phys. Status Solidi B* **2008**, *245*, 761–768.
52. Zubko, P.; Catalan, G.; Buckley, A.; Welche, P. R. L.; Scott, J. F. Strain-Gradient-Induced Polarization in $SrTiO_3$ Single Crystals. *Phys. Rev. Lett.* **2007**, *99*, 16−7601–167601−4.
53. Lee, J.; Choi, C. H.; Park, B. H.; Noh, T. W.; Lee, J. K. Built-in Voltages and Asymmetric Polarization Switching in $Pb(Zr,Ti)O_3$ Thin Film Capacitors. *Appl. Phys. Lett.* **1998**, *72*, 3380–3382.
54. Resta, R. Towards a Bulk Theory of Flexoelectricity. *Phys. Rev. Lett.* **2010**, *105*, 127601–127601−4.
55. Takayama, R.; Tomita, Y. Preparation of Epitaxial $Pb(Zr_xTi_{1-X})O_3$ Thin Films and their Crystallographic, Pyroelectric, and Ferroelectric Properties. *J. Appl. Phys.* **1989**, *65*, 1666–1670.
56. Tagantsev, A. K. Electric Polarization in Crystals and its Response to Thermal and Elastic Perturbations. *Phase Transitions* **1991**, *35*, 119–203.
57. Narayanan, M.; Tong, S.; Liu, S.; Ma, B.; Balachandran, U. Estimation of Intrinsic Contribution to Dielectric Response of $Pb_{0.92}La_{0.08}Zr_{0.52}Ti_{0.48}O_3$ Thin Films at Low Frequencies using High Bias Fields. *Appl. Phys. Lett.* **2013**, *102*, 062906–062906−4.
58. Nakamura, K.; Kawamura, Y. Orientation Dependence of Electromechanical Coupling Factors in $KNbO_3$. *IEEE Trans. Ultrason., Ferroelect., Freq. Control* **2000**, *47*, 750–755.
59. Sebald, G.; Lefeuvre, E.; Guyomar, D. Pyroelectric Energy Conversion: Optimization Principles. *IEEE Trans. Ultrason., Ferroelect., Freq. Control* **2008**, *55*, 538–551.
60. Wang, Q.; Du, X.; Xu, B.; Eric Cross, L. Electromechanical Coupling and Output Efficiency of Piezoelectric Bending Actuators. *IEEE Trans. Ultrason., Ferroelect., Freq. Control* **1999**, *46*, 638–646.
61. Navid, A.; Pilon, L. Pyroelectric Energy Harvesting using Olsen Cycles in Purified and Porous Poly(Vinylidene Fluoride-Trifluoroethylene) [P(VDF-TrFE)] Thin Films. *Smart Mater. Struct.* **2011**, *20*, 025012–025012−9.
62. Sebald, G.; Seveyrat, L.; Guyomar, D.; Lebrun, L.; Guiffard, B.; Pruvost, S. Electrocaloric and Pyroelectric Properties of $0.75Pb(Mg_{1/3}Nb_{2/3})O_3-0.25PbTiO_3$ Single Crystals. *J. Appl. Phys.* **2006**, *100*, 124112–124112−6.
63. Vrejoiu, I.; LeRhun, G.; Pintilie, L.; Hesse, D.; Alexe, M.; Gösele, U. Intrinsic Ferroelectric Properties of Strained Tetragonal $PbZr_{0.2}Ti_{0.8}O_3$ Obtained on Layer-by-Layer Grown, Defect-Free Single-Crystalline Films. *Adv. Mater.* **2006**, *18*, 1657–1661.
64. Damjanovic, D.; Demartin, M. Contribution of the Irreversible Displacement of Domain Walls to the Piezoelectric Effect in Barium Titanate and Lead Zirconate Titanate Ceramics. *J. Phys.: Condens. Matter* **1997**, *9*, 4943–4953.
65. Hall, D. A. Rayleigh Behaviour and the Threshold Field in Ferroelectric Ceramics. *Ferroelectrics* **1999**, *223*, 319–328.
66. Karthik, J.; Damodaran, A. R.; Martin, L. W. Effect of 90° Domain Walls on the Low-Field Permittivity of $PbZr_{0.2}Ti_{0.8}O_3$ Thin Films. *Phys. Rev. Lett.* **2012**, *108*, 167601–167601−5.
67. Karthik, J.; Damodaran, A. R.; Martin, L. W. Epitaxial Ferroelectric Heterostructures Fabricated by Selective Area Epitaxy of $SrRuO_3$ using an MgO Mask. *Adv. Mater.* **2012**, *24*, 1610–1615.